Supporting Information

Gold Metal Liquid-Like Droplets

*Evgeny Smirnov,[†,§] Micheál D. Scanlon,[†,§] Dmitry Momotenko,[†] Heron Vrubel,[†] Manuel A. Méndez,[†] Pierre-Francois Brevet[‡] and Hubert H. Girault[†,]**

†Laboratoire d'Electrochimie Physique et Analytique, Ecole Polytechnique Fédérale de Lausanne, Station 6, CH-1015 Lausanne, Switzerland.

‡Institut Lumière Matière, ILM UMR CNRS 5306, Universite Claude Bernard Lyon 110 Rue Ada Byron, 69622 Villeurbanne Cedex, France.

Table of Contents

SI-1: Descriptions of the Supporting Movies highlighting gold metal liquid-like droplet (MeLLD) formation

Movie S1. Preparation of a gold metal-like liquid droplets (MeLLDs) consisting of 14 nm mean diameter AuNPs. The whole procedure outlined in Figure 5 is shown in real time and it clearly takes less than 60s to complete. The reflective gold MeLLD formed is reddish/brown in color.

Movie S2. Preparation of a gold MeLLD consisting of 76 nm mean diameter AuNPs. The gold MeLLDs formed clearly have the characteristics of "bulk gold" in terms of color and reflectivity.

Movie S3. This movie is a direct continuation of movie S3 where the colorless aqueous phase, that previously contained colloidal AuNPs, is removed and additional aliquots of a 76 nm aqueous AuNP colloidal solution are added to the cell. The purpose of this film is to show that multilayer formation is possible by simply replacing the aqueous phase with a fresh AuNP solution and repeating the procedure shown in movies S1 and S2 repeatedly**.**

Movie S4. This movie shows a DCE droplet coated in a gold metal liquid-like film dropping through the narrow eye of an hourglass. The purpose of this video is to highlight the "liquid gold" behavior of the films. They are clearly deformable and the gold MeLLDs can be destroyed by shaking but reformed by allowing the system to settle momentarily.

Movie S5. This movie highlights the repeatable reversible deformation of a gold MeLLD upon compression (by withdrawing DCE using a micropipette) and subsequent decompression (by expanding the volume of the droplet on re-injecting the DCE). The reversible loss and retention of spectral reflectivity is unusual and characteristic of the flexible but cohesive nature of the continuous interface TTF film that encases the AuNPs at the liquid-liquid interface.

SI-2: Characterization by transmission electron microscopy (TEM) and scanning electron microscopy (SEM)

The morphologies of the AuNPs in each colloidal solution were examined by transmission electron microscopy (TEM; Figure S1). The as-prepared AuNP solutions were dropped onto standard carbon-coated copper grids (200-mesh) and air-dried for about 2 hours. The TEM images were obtained using a FEI CM12 (Phillips) transmission electron microscope, operating with a LaB_6 electron source at 120 kV. The average size distributions of the AuNPs, with an assumption made that the AuNPs are prefect spheres, were determined on the basis of the TEM images with the use of ImageJ software. For each sample in excess of 160 AuNPs were analyzed (taken from 4 to 5 individual TEM images). The mean diameters (d / nm) of the smaller and larger AuNPs were 13 ± 1 and 65 ± 10 nm, respectively (Figure S1).

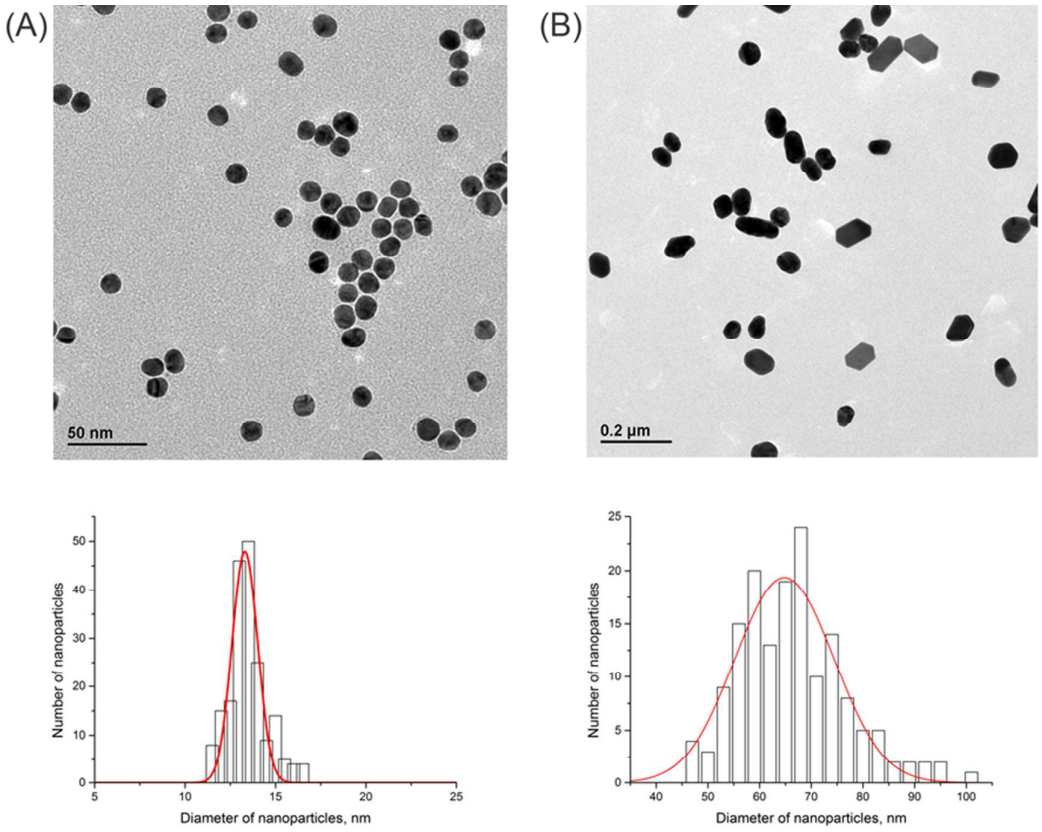

Figure S1. TEM images of **(A)** the smaller and **(B)** the larger colloidal AuNPs with their size distributions underneath (the red curves are Gaussian approximations of the size distributions).

The morphologies and packing arrangement of the gold MeLLDs formed with the smaller and larger AuNPs were investigated both by TEM and SEM. The AuNPs

were transferred to either standard carbon-coated copper grids (200-mesh, for TEM analysis) or a silicon substrate (for SEM analysis) by carefully touching the surface of the macroscopic gold MeLLDs. The smooth silicon substrate was treated with oxygen plasma (Diener Femto Plasma System) for 15 minutes prior to film transfer. This both ensured maximum cleanliness of the surface and the presence of a hydrophilic SiO_2 layer. The hydrophilicity of the SiO_2 layer was crucial to ensure the hydrophilic liquid gold film transferred to the solid substrate without complication.

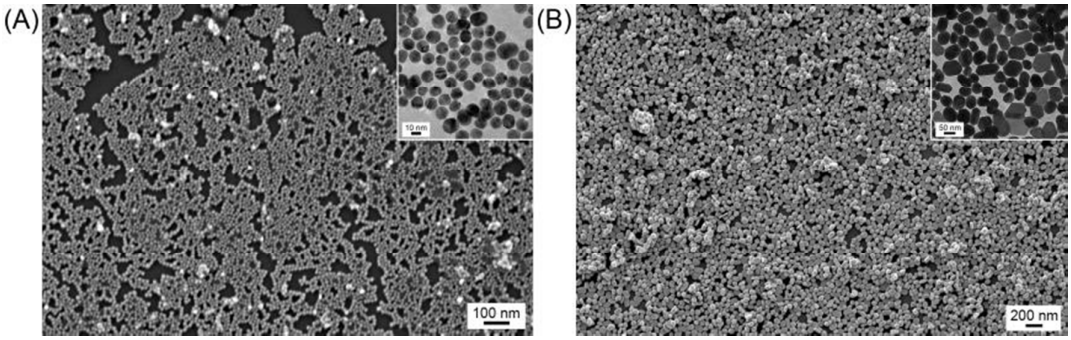

Figure S2. SEM images of liquid gold films prepared with (A) the smaller and (B) the larger AuNPs after transfer to smooth silicon substrates. The samples were transferred from gold MeLLDs of approximate monolayer coverage. The insets are TEM images of the corresponding samples on standard carbon-coated copper grids.

As clearly illustrated in Figure S2, A and B, the spatial arrangements of the AuNPs in each film appear quite dense. Cracks are evident for the films formed with the smaller AuNPs (Figure S2A) and may have been formed during the transfer process. The beginnings of multilayer formation are evident for the larger AuNPs with isolated areas containing stacks of AuNPs (Figure S2B). The TEM images, inset, are informative, giving clear evidence that the majority of the AuNPs do not touch each other and are separated by small 1 or 2 nm gaps. These gaps are likely to be filled with the "interfacial glue" of TTF (invisible to TEM) described in detail in the main text (Figure 5E).

SI-3: Characterization by UV/vis spectroscopy, zeta (ζ)-potential and dynamic light scattering measurements

An alternative method of determining the mean diameters and approximate concentrations of the colloidal AuNP solutions was to employ UV/vis spectroscopy, as detailed by Haiss *et al.*[1] Briefly, for AuNPs with mean diameters in the range 35 – 110 nm, Haiss *et al.* developed Equation S1 and Equation S2 that have an average absolute deviation in calculating the mean experimentally observed AuNP diameters (d / nm) of only ~3%,

$$\lambda_{\mathrm{LSPR}} = \lambda_0 + L_1 \exp(L_2 d) \qquad \text{(S1)}$$

$$d = \frac{\ln\left(\frac{\lambda_{\mathrm{LSPR}} - \lambda_0}{L_1}\right)}{L_2} \qquad \text{(S2)}$$

where λ_{LSPR} is the experimentally observed localized surface plasmon resonance (LSPR) extinction peak for the AuNP solution, and λ_0 (512 nm), L_1 (6.53) and L_2 (0.0216) are Haiss *et al.*'s theoretical fit parameters for d > 25 nm. From the UV/vis spectra in Figure 2A, λ_{LSPR} for the larger AuNPs was 545.7 nm which corresponds to d = 76 nm. For AuNPs with mean diameters < 25 nm, as was the case for our smaller AuNPs, Haiss *et al.* developed an alternative approach to determine d (Equation S3). The underlying premise is based on the fact that as the size of the AuNPs decreases, the magnitude of their absorbance at their localized surface plasmon resonance (A_{LSPR}) is damped (due to the reduced mean free path of the electrons) relative to the absorbance at other wavelengths. Thus, Haiss *et al.* show that the ratio of A_{LSPR} to the absorbance at 450 nm (A_{450}) is dependent on the logarithm of d for AuNPs in the size range 5 – 80 nm. The specific absorbance at 450 nm gave the best fit between theory and experimentally observed values of d as (i) in the long-wavelength range the mean free path of the electrons has a more pronounced influence on the optical functions, and (ii) the presence of small quantities of oblate AuNPs or aggregates in some colloidal solutions show strong absorbance at longer wavelengths and introduce error.

$$d = \exp\left(B_1 \frac{A_{\mathrm{LSPR}}}{A_{450}} - B_2\right) \qquad \text{(S3)}$$

where B_1 (3.00) and B_2 (2.20) are their experimentally determined fit parameters that give an average absolute deviation of calculating d of ~11%. From the UV/vis spectra

in Figure 2A, A_{LSPR} and A_{450} were 1.246 and 0.776, respectively, for the smaller AuNPs which corresponds to d = 14 nm. Once d has been determined by either Equation S2 or S3, and making a reasonable assumption that the citrate-coated AuNPs can be described as uncoated AuNPs, as citrate is a small molecule known to lie flat on Au(111),[2] Haiss *et al.* have furthermore shown that the number density of AuNPs (N_{AuNPs}) can be calculated using Equation S4 from the A_{450} values with an average deviation of ~6%,

$$N_{AuNPs} = \frac{A_{450} \times 10^{14}}{d^2 \left[-0.295 + 1.36 \exp\left(-\left(\frac{d - 96.8}{78.2} \right)^2 \right) \right]} \qquad \text{(S4)}$$

Equation S4 was derived using the fit parameters for an equation relating the calculated values of the extinction efficiency (Q_{ext}) of the AuNPs at a wavelength of 450 nm as a function of d over the full range of AuNP sizes. For the larger AuNPs (d = 76, A_{450} = 0.757) N_{AuNPs} was calculated as 1.35×10^{10} AuNPs·mL^{-1}, while for the smaller AuNPs (d = 14, A_{450} = 0.776) N_{AuNPs} was calculated as 2.67×10^{12} AuNPs·mL^{-1}. Finally, Haiss *et al.* have provided values of the molar extinction coefficient of the AuNPs at 450 nm (ε_{450} / L·mol^{-1}·cm^{-1}), as a function of d, and the concentration of AuNPs (c_{AuNPs} / mol·L^{-1}), can be calculated with Equation S5, using an optical path length, l, of 1 cm,

$$c_{AuNPs} = \frac{A_{450}}{\varepsilon_{450}} \qquad \text{(S5)}$$

For the larger AuNPs (d = 76, ε_{450} = 3.4×10^{10} L·mol^{-1}·cm^{-1}, A_{450} = 0.757) c_{AuNPs} was calculated as 0.022×10^{-9} mol·L^{-1}, while for the smaller AuNPs (d = 14, ε_{450} = 2.67×10^{8} L·mol^{-1}·cm^{-1}, A_{450} = 0.776) c_{AuNPs} was calculated as 2.906×10^{-9} mol·L^{-1}. A summary of the characteristics of both aqueous colloidal AuNP solutions, determined both by TEM and UV/vis spectroscopic analysis, is presented in Table S1.

Table S1. Characteristics of the synthesized aqueous colloidal AuNP solutions.

	λ_{SPR} (nm)	A_{LSPR}	A_{450}	d, UV/vis (nm)	d, TEM (nm)	N_{AuNPs} (AuNPs·mL^{-1})	ε_{450} (L·mol^{-1}·cm^{-1})	c_{AuNPs} (mol·L^{-1})
Smaller AuNPs	520.0	1.246	0.776	14	13 (± 1)	2.67×10^{12}	2.67×10^{8}	2.906×10^{-9}
Larger AuNPs	545.7	1.508	0.757	76	65 (±10)	1.35×10^{10}	3.4×10^{10}	0.022×10^{-9}

On contacting the two phases in Figure 1A, charge transfer occurs between the AuNP and the TTF molecule and citrate is subsequently displaced at the AuNP surface by $TTF^{\bullet+}_{ads}$. Thus, the Coulombic repulsive forces are considerably lessened compared to those of citrate stabilized AuNPs. This is the key factor than induces bulk AuNP aggregation in our system as indicated by ζ-potential and DLS measurements summarized in Table S2.

Table S2. Summary of ζ-potential and DLS measurements of as prepared citrate coated and $TTF^{\bullet+}_{ads}$ aggregated AuNP solutions.

	Smaller (14 nm) AuNPs		Larger (76 nm) AuNPs	
	As prepared	Aggregated	As prepared	Aggregated
ζ-potential (mV)	–43 ± 12	–25 ± 8	–37 ± 11	–12 ± 8
Particle Sizes Observed (nm)	22 ± 8	885 ± 372	68 ± 27	378 ± 196 & > 4000

SI-4: Estimation of the interfacial coverage

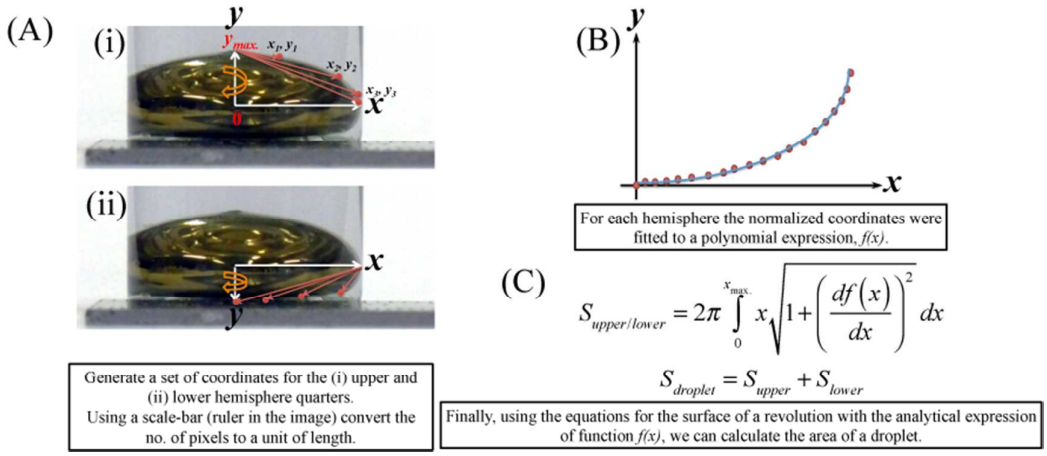

Figure S3. Procedure to determine the surface area of a droplet, $S_{droplet}$.

The surface area of the droplet, $S_{droplet}$, was determined in three steps, see Figure S3. (A) Firstly, the droplet was carefully photographed, ensuring the absence of any optical distortions. Next, the coordinates for the extremities of the droplet surface were determined using Adobe Photoshop CS5 software. The sphere was divided into an upper and lower hemisphere. For each hemisphere the coordinates were recorded for one half of that hemisphere. The coordinates were normalized using a scale bar provided by a ruler in the photograph (with each pixel representing a specific length). (B) Once these coordinates were determined, a polynomial function for each hemisphere, *f(x)*, was generated. (C) Finally, using the expressions for the surface of a revolution in Figure S3, the surface areas of each hemisphere were determined individually (by rotation around the *y*-axis), and subsequently the total area of the droplet, $S_{droplet}$, was calculated. These calculations were performed using Mathematica software (version 8.0).

The surface area occupied by an individual AuNP under monolayer conditions is determined by the packing arrangement of the AuNPs. Here, we calculate the areas occupied by the AuNPs assuming either a square close packing (SCP) or hexagonal close packing (HCP) arrangement. The surface areas occupied by a single AuNP with SCP ($S_{AuNP,\ SCP}$) or HCP ($S_{AuNP,\ HCP}$) are given by Equation S6 and Equation S7, respectively,

$$S_{AuNP,\ SCP} = d^2 \qquad \text{(S6)}$$

$$S_{\text{AuNP, HCP}} = \frac{\sqrt{3}d^2}{2} \qquad \text{(S7)}$$

where d is the mean diameter of the AuNPs in a colloidal solution. The values of d for both AuNP colloidal solutions were determined using the methods of Haiss *et al.*[1] discussed earlier, and thus $S_{\text{AuNP, SCP}}$ and $S_{\text{AuNP, HCP}}$ are known. Next, we can calculate the number of AuNPs required to coat the surface of our droplet with a perfect monolayer (N_{mono}) depending on the packing arrangement. Taking the case for SCP, we get Equation 8,

$$N_{\text{mono, SCP}} = \frac{S_{droplet}}{S_{\text{AuNP, SCP}}} \qquad \text{(S8)}$$

Earlier, using Haiss *et al.*'s[1] treatment of the UV/vis data we were also able to determine the number density of AuNPs per mL (N_{AuNPs}) of our colloidal stock solutions. Thus, we are now in a position to determine the volumes of our stock aqueous colloidal solutions that are required to cover the surface of our oil droplet with a perfect monolayer, V_{mono}, again taking the case for SCP,

$$V_{\text{mono, SCP}} = \frac{N_{\text{mono, SCP}}}{N_{\text{AuNPs}}} \qquad \text{(S9)}$$

Finally, the surface coverage is expressed as a monolayer fraction (S_{mono}), that depends on the packing arrangement, d, N_{AuNPs}, and V_{mono}, for a known volume of added AuNP colloidal solution (V_{add}) may be determined using Equation (S10),

$$S_{\text{mono, SCP}} = \frac{V_{\text{add}}}{V_{\text{mono, SCP}}} \qquad \text{(S10)}$$

The monolayer fraction surface coverage, assuming either SCP or HCP, for the gold film coated droplets shown in Figure 1E and Figure 1F are given in Table S2. The surface coverage's for the data presented in Figure 2B (outlining the changes in UV/vis response of the liquid gold film depending on surface coverage) are given in Table S3.

Table S3. Estimation of the monolayer fraction surface coverage's (S_{mono}) for the gold MeLLDs shown in Figure 1E (d = 14 nm, N_{AuNPs} = 2.67×10^{12} AuNPs·mL^{-1}) and Figure 1F (d = 76 nm, N_{AuNPs} = 1.35×10^{10} AuNPs·mL^{-1}), respectively, depending on assumed packing arrangement.

d (nm)	V_{add} (mL)	$S_{mono,\ SCP}$	$S_{mono,\ HCP}$
14	0.1	0.07	0.06
	0.25	0.17	0.15
	0.5	0.34	0.30
	1	0.69	0.60
	2	1.38	1.20
	5	3.45	2.29
76	1	0.01	0.09
	2	0.20	0.18
	4	0.41	0.35
	6	0.61	0.53
	8	0.82	0.71
	35	3.58	3.11

Table S4. Estimation of the monolayer fraction surface coverage's (S_{mono}) for the gold MeLLDs analyzed by UV/vis spectroscopy in a quartz cuvette ($S_{droplet}$ ≈ 6 cm^2) in Figure 2B (d = 14 nm, N_{AuNPs} = 2.68×10^{12} AuNPs·mL^{-1}) depending on assumed packing arrangement.

d (nm)	V_{add} (mL)	$S_{mono,\ SCP}$	$S_{mono,\ HCP}$
14	0.2	0.17	0.15
	0.3	0.26	0.23
	0.4	0.35	0.30
	0.5	0.44	0.38
	0.6	0.52	0.45
	0.7	0.61	0.53
	0.8	0.70	0.61
	0.9	0.79	0.68
	1.0	0.88	0.79
	1.1	0.96	0.83

SI-5: Control Experiments

SI-5A: Analysis of the aqueous and DCE phases pre-and post-gold MeLLD formation

The aqueous and DCE phases were studied by UV/vis spectroscopy pre- and post-gold MeLLD formation. UV/vis spectra were obtained as described in the Experimental Section of the main text. The spectra revealed that no colloidal AuNPs were present in either phase post-gold MeLLD formation (with both colloidal AuNP stock solutions), clearly indicating that all AuNPs were confined to the interfacial region (Figure S4). The aqueous phase was completely blank post-gold MeLLD formation whereas the DCE phase gave identical responses, characteristic of neutral TTF,[3] pre- and post-gold MeLLD formation for both AuNP stock solutions.

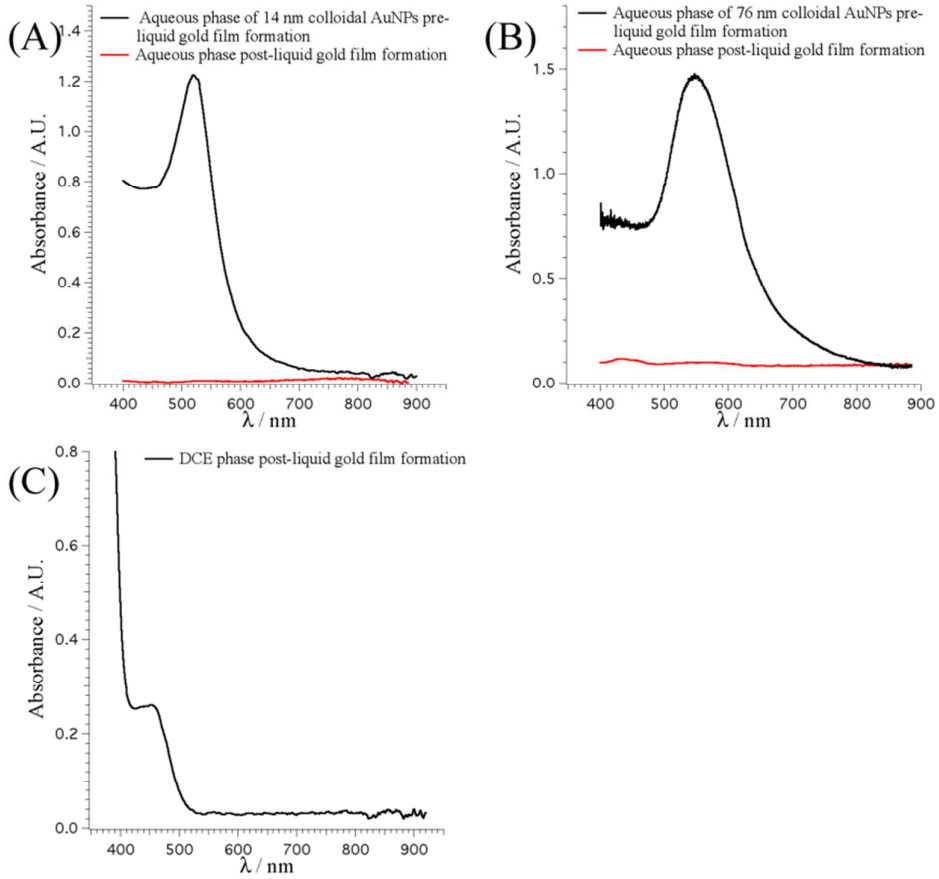

Figure S4. UV/vis spectra highlighting the complete absence of colloidal AuNPs from the aqueous phases for **(A)** the 14 nm and **(B)** the 76 nm colloidal AuNP solutions; and **(C)** from the DCE phase for the 76 nm AuNPs, post-liquid gold film formation. Thus, by inference all of the AuNPs originally in the aqueous colloids for both AuNP sizes were now confined to their respective interfacial liquid gold films.

SI-5B: Highlighting the role of neutral TTF in the DCE phase to induce AuNP aggregation, and hence MeLLD formation

A control experimental was performed to highlight the fact that in the absence of TTF in the DCE phase the aqueous colloidal AuNP solutions remain stable and unaggregated with time. These experiments were performed with the 76 nm colloidal AuNP solution as, being larger, these AuNPs precipitated more quickly, allowing the full data set to be obtained in a much shorter time-frame than would be the case for the smaller 14 nm AuNP solutions. Thus, potential experimental problems, associated with evaporation or a loss of stability of the UV/vis response over very long timescales of continuous use, were avoided. Kinetic experiments were monitored by UV/vis spectroscopy, as described in the Experimental Section of the main text. As highlighted (Figure 2, C and D; Figure S5), TTF initially induced the AuNPs to aggregate giving rise to an increase in absorbance at λ_{SPR} = 760 nm and a decrease in absorbance at λ_{LSPR} = 545 nm, for 76 nm AuNPs. After this initial 40-minute period, the AuNP aggregates grew larger and began to precipitate under the influence of gravity, thereby leading to decreases in absorbance at both 545 and 760 nm (Figure 2D). No such trends were observed in the absence of TTF (Figure S5C).

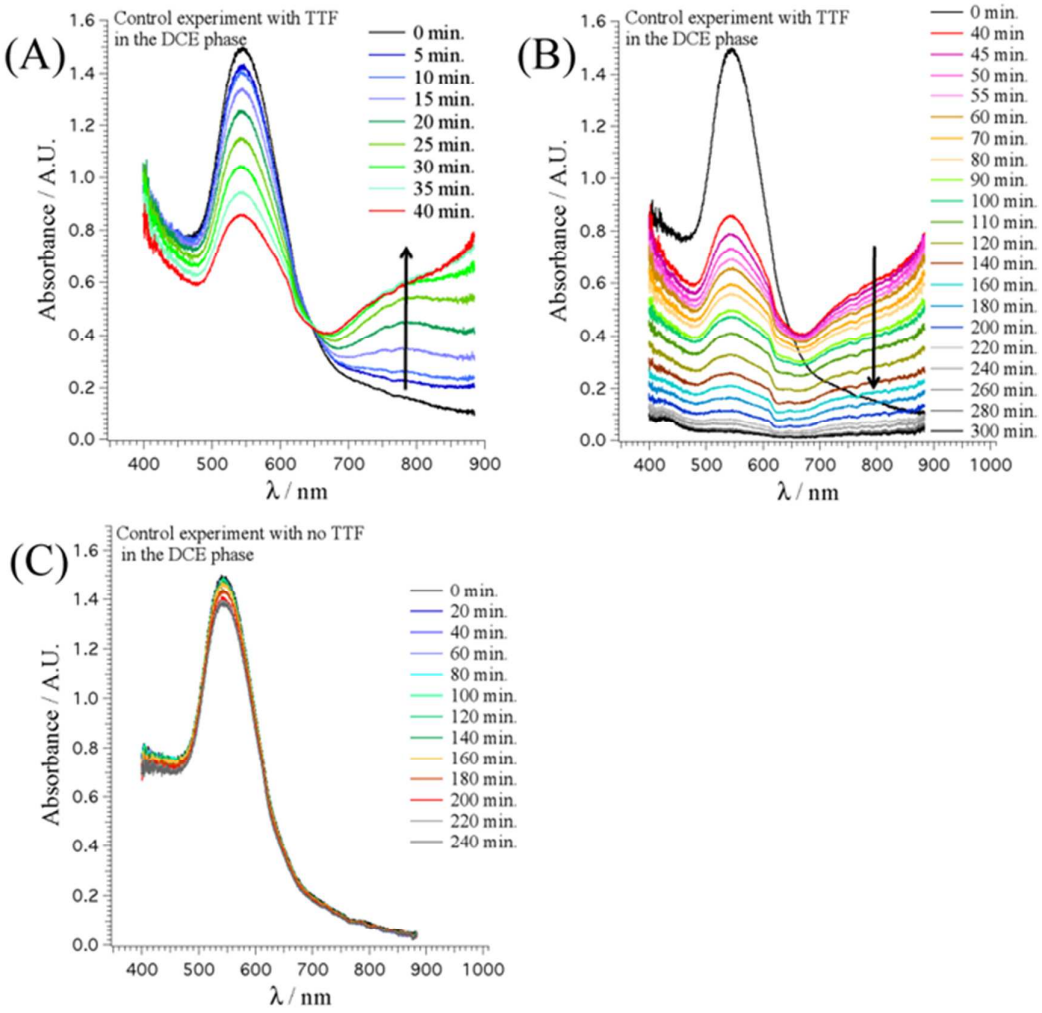

Figure S5. The influence of TTF in the DCE oil phase on the kinetics of aggregation and precipitation of 76 nm colloidal AuNPs. UV/vis spectra were taken of the aqueous phase slightly above the interface at regular 5-minute intervals. The kinetic behavior of the 76 nm AuNPs, with an extinction peak at λ_{LSPR} = 545 nm, that **(A)** firstly aggregated, giving rise to an increase in absorbance at λ_{SPR} = 760 nm and a decrease in absorbance at λ_{LSPR} = 545 nm, and **(B)** subsequently precipitated, decreasing the absorbance at both 545 and 760 nm, was monitored. **(C)** A control experiment was performed without TTF in a DCE oil phase in contact with the 76 nm AuNPs. No aggregation and precipitation was seen on contacting the colloidal AuNP solution in the absence of TTF. All kinetic experiments were carried out under quiescent conditions in air.

SI-5C: The importance of emulsification; no gold MeLLDs form under quiescent conditions

AuNP aggregation can occur through, and switch between, two possible mechanistic routes depending on the AuNP concentration.[4-5] Aggregates may form primarily by the addition of single AuNPs to form clusters, or various clusters may combine to form even larger clusters.[4-5] As noted in the main article, vigorous shaking of the reaction cell prevents the formation of large aggregates of AuNPs by rapidly facilitating the spontaneous absorption of individual, and small aggregates of, $TTF^{\bullet+}_{ads}$ coated AuNPs to the interface. In the absence of emulsification, gold MeLLDs do not form (Figure S6), with large black AuNP aggregates instead precipitating with time onto the interface and onto the bottom of the reaction vial.

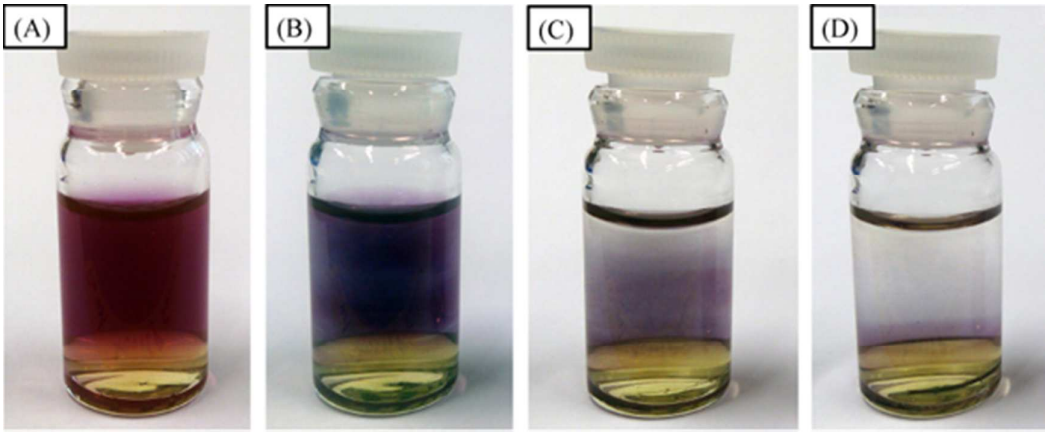

Figure S6. The appearance of the colloidal solution of 14 nm AuNPs visibly changes due to aggregation and precipitation after **(A)** 0, **(B)** 50, **(C)** 125 and **(D)** 225 minutes of reaction with a 1 mM TTF solution in DCE in the absence of vigorously shaking the cell. The kinetics of these slow color changes were followed by UV/vis spectroscopy in a quartz cuvette earlier in Figure S5, A and B.

Also, vigorously shaking the biphasic system after extensive AuNP aggregation had occurred (such as in Figure S6, B and C) failed to induce the formation of gold MeLLDs, emphasizing the importance of capturing the small AuNP aggregates quickly.

SI-5D: Investigating the conductivity of gold MeLLDs by electrochemical impedance spectroscopy (EIS)

The discussion and experimental details of this experiment are provided in the Results and Discussion and Experimental Sections of the main article.

Table S5: Values of the equivalent circuit elements described in Figure 3, main text.

Cell	R_1 (MΩ)	R_2 (MΩ)	CPE_1 (x 10^{-6} $F^{-1}.s^{1-n}$)	n_1	% error in fitting
14 nm liquid gold film	0.147	1.305	1.529	0.7142	< 1.979
76 nm liquid gold film	0.230	13.280	0.8204	0.7772	< 2.578
Bare water-DCE interface	1.409	11.920	1.101	0.8354	< 0.869
Pure water	1.727	15.450	1.734	0.8207	< 1.976
1 mM TTF in DCE	3.866	9.205 x 10^9	0.971	0.4989	< 1.173

SI-6: Supporting notes on the mechanism of metal liquid-like droplet (MeLLD) formation

SI-6A: Elucidating the DCE/water partition coefficient of neutral TTF^0

Currently, data is only available for the *n*-octanol/water partition coefficient of TTF^0 ($\log P_{\text{octanol/w}} = 3.019$). However, we have investigated the relationship between $\log P_{\text{DCE/w}}$ and $\log P_{\text{octanol/w}}$ previously, and identified the major difference between them as the expression of the H-bonding capacity of the solutes.[6] Non-H-bond donors, such as TTF^0, were found to be more lipophilic in DCE/water than in *n*-octanol/water and a $\log P_{\text{DCE/w}}$ in excess of 4 is expected. Thus, as little as 1 in every 10,000 molecules of TTF^0 will partition to water phase, with nanomolar quantities of TTF^0_{w} available for reaction with colloidal AuNPs in the bulk water.

SI-6B: Discussion of homogeneous and heterogeneous charge transfer between TTF^0 and AuNPs

Immediately after placing the aqueous and DCE phases in contact, neutral TTF^0 molecules partition between the oil (TTF^0_{oil}) and water (TTF^0_{w}) phases, with as little as 1 in every 10,000 molecules of TTF^0 partitioning to water. Therefore, a small portion $(s+q)$, in the nanomolar range, of the total $(n+p+s+q)$ TTF^0 present initially is available for homogeneous reaction with the AuNPs in the bulk aqueous phase (*n, p, s* and *q* are defined *vide infra*)

$$(n+p+s+q)\text{TTF}^0_{\text{oil}} \rightarrow (n+p)\text{TTF}^0_{\text{oil}} + (s+q)\text{TTF}^0_{\text{w}} \qquad \text{(S11)}$$

Thus, in our system (Figure 1A), the charge transfer between the TTF^0 and the AuNP and, the ensuring displacement of citrate from the negatively charged AuNP with the electrostatically adsorbed $TTF^{\bullet+}$, may occur both homogeneously in bulk water (Equation S12) and heterogeneously at the interface (Equation S13),

$$(\text{AuNP}^z_{\text{w}} : m\ \text{cit}^{3-}_{\text{ads}})^{z-3m} + (s+q)\text{TTF}^0_{\text{w}} \rightarrow (\text{AuNP}^{z-s-q}_{\text{w}} : s\ \text{TTF}^{\bullet+}_{\text{ads}})^{z-q} + m\ \text{cit}^{3-}_{\text{w}} + q\ \text{TTF}^{\bullet+}_{\text{w}} \qquad \text{(S12)}$$

$$(\text{AuNP}^z_{\text{w}} : m\ \text{cit}^{3-}_{\text{ads}})^{z-3m} + (n+p)\text{TTF}^0_{\text{oil}} \rightarrow (\text{AuNP}^{z-n-p}_{\text{int}} : n\ \text{TTF}^{\bullet+}_{\text{ads}})^{z-p} + m\ \text{cit}^{3-}_{\text{w}} + p\ \text{TTF}^{\bullet+}_{\text{w}} \qquad \text{(S13)}$$

where z represents the electronic charge on the core of the AuNP (z is likely to be positive due to the incomplete reduction of gold atoms at the AuNP surface by citrate during synthesis, *i.e.,* a core-shell structure exists with a positively charged AuNP surface and a surrounding negative layer of citrate), m is the number of citrate (cit) ligands per AuNP, n and s are the number of oxidized TTF molecules assumed to remain adsorbed ($TTF^{\bullet+}_{ads}$) to the AuNP surface at the interface (int) or in bulk water (w), respectively, and p and q are the number of $TTF^{\bullet+}_{ads}$ molecules at the interface or in the bulk water, respectively, that subsequently desorb from the AuNP surface and partition to the aqueous phase ($TTF^{\bullet+}_{w}$). A graphical description of Equation S11 to Equation S13 is illustrated in Figure S7.

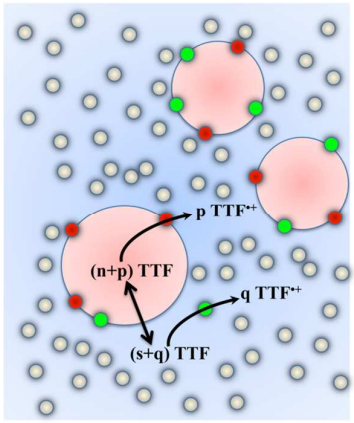

Figure S7. A graphical illustration of the homogeneous and heterogeneous charge transfer reactions occurring between neutral TTF and AuNPs, resulting in the formation of free $TTF^{\bullet+}$ and $TTF^{\bullet+}_{ads}$ coated AuNPs (the green AuNPs correspond to those that underwent a homogeneous reaction and are either still free in the aqueous phase or subsequently trapped at the interface, while the red AuNPs are those that react heterogeneously at the interface).

The surface of the AuNP is a dynamic environment with an equilibrium existing between $TTF^{\bullet+}_{ads}$ and free $TTF^{\bullet+}$ in solution. Taking into consideration the substantially higher solubility of $TTF^{\bullet+}$ than TTF^{0} in bulk water and the ease with which $TTF^{\bullet+}$ can cross the water-oil interface, as illustrated by the standard ion transfer potential of $TTF^{\bullet+}$, $\Delta\phi^{0,\,oil\rightarrow w}_{tr.,TTF^{\bullet+}}$, being –0.020 V (determined by ion transfer voltammetry experiments at a polarized water-DCE interface),[3] it is likely that portions of the oxidized $TTF^{\bullet+}$ generated both homogeneously and heterogeneously

are available to coat AuNPs in the aqueous phase, further displacing citrate ligands without previous charge injection into the AuNP (Equation S14).

$$(\mathrm{AuNP}_{\mathrm{w}}^{z} : m\ \mathrm{cit}_{\mathrm{ads}}^{3-})^{z-3m} + (p+q)\mathrm{TTF}_{\mathrm{w}}^{\bullet+} \rightarrow (\mathrm{AuNP}_{\mathrm{w}}^{z} : \left(p+q\right)\ \mathrm{TTF}_{\mathrm{ads}}^{\bullet+})^{z-(p+q)} + m\ \mathrm{cit}_{\mathrm{w}}^{3-} \qquad \text{(S14)}$$

SI-6C: The reduction potentials of TTF^0 in water and DCE on the absolute vacuum scale (AVS)

The reduction potential of TTF_{oil}^{0}, where the oil is DCE, with respect to the Standard Hydrogen Electrode (SHE), $\left[E^{0}_{\mathrm{TTF}^{\bullet+}/\mathrm{TTF}}\right]^{\mathrm{oil}}_{\mathrm{SHE}}$, is 0.560 V.[3] The standard ion transfer potential of $TTF^{\bullet+}$, $\Delta^{\mathrm{w}}_{\mathrm{o}}\phi^{0}_{\mathrm{tr,TTF}^{\bullet+}}$, determined by ion transfer voltammetry experiments at a polarized water-DCE interface, is –0.020 V.[3] Thus, as $\log P_{\mathrm{DCE/w}}$ for TTF^0 is ~4, the reduction potential of TTF_{w}^{0} with respect to SHE, $\left[E^{0}_{\mathrm{TTF}^{\bullet+}/\mathrm{TTF}}\right]^{\mathrm{w}}_{\mathrm{SHE}}$, elucidated using the thermodynamic cycle shown in Figure S8 and Equation S15, is –0.303 V.

$$\Delta G^{0,\mathrm{w}}_{\mathrm{TTF}^{\bullet+}/\mathrm{TTF}^{0}} = \Delta G^{0,\mathrm{w}\rightarrow\mathrm{oil}}_{tr.,\,\mathrm{TTF}^{0}} + \Delta G^{0,\mathrm{oil}}_{\mathrm{TTF}^{0}/\mathrm{TTF}^{\bullet+}} + \Delta G^{0,\mathrm{w}\rightarrow\mathrm{oil}}_{tr.,\,\mathrm{TTF}^{\bullet+}} \qquad \text{(S15)}$$

where $\Delta G^{0,\mathrm{w}}_{\mathrm{TTF}^{\bullet+}/\mathrm{TTF}^{0}}$, $\Delta G^{0,\mathrm{w}\rightarrow\mathrm{oil}}_{tr.,\,\mathrm{TTF}^{0}}$, $\Delta G^{0,\mathrm{oil}}_{\mathrm{TTF}^{0}/\mathrm{TTF}^{\bullet+}}$ and $\Delta G^{0,\mathrm{w}\rightarrow\mathrm{oil}}_{tr.,\,\mathrm{TTF}^{\bullet+}}$ are the standard Gibbs energies of reduction of $TTF^{\bullet+}$ in water, transfer of TTF^0 from water to oil, oxidation of TTF^0 in oil and ion transfer of $TTF^{\bullet+}$ from oil to water, respectively.

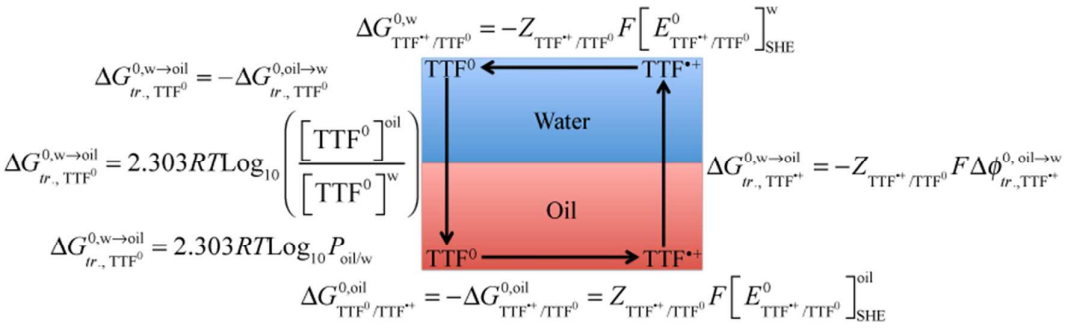

Figure S8. Thermodynamic cycle used to determine the reduction potential of aqueous $TTF^{\bullet+}$.

The potentials on the SHE scale are related to the Absolute Vacuum Scale (AVS) by 4.440 eV,[7] giving us $\left[E^0_{TTF^{\bullet+}/TTF}\right]^{w}_{AVS}$ and $\left[E^0_{TTF^{\bullet+}/TTF}\right]^{oil}_{AVS}$ as 4.137 and 5.000 V, respectively. The work function of bare gold is 5.320 V *vs.* AVS,[8] and we assume that ϕ_{AuNP} does not deviate substantially from this value for citrate stabilized AuNPs, or subsequently, on adsorption of TTF^0.

SI-6D: Bulk inter-particle interactions that counteract Coulombic repulsion

$TTF^{\bullet+}_{ads}$ is an aromatic molecule, in terms of the Hückel definition, due to the 6π heteroaromaticity of the 1,3-dithiolium cation.[9] As mentioned above, this aromaticity is only possible as the $TTF^{\bullet+}_{ads}$ ligands do not covalently bond to the AuNP surface. Thus, $TTF^{\bullet+}_{ads}$ ligands adsorbed on neighboring AuNPs can in principle undergo intermolecular π – π interactions, in addition to non-bonding S – S interactions.[9] Typically, π – π interactions are between two closed-shell molecules, however, for $TTF^{\bullet+}_{ads}$ – $TTF^{\bullet+}_{ads}$ interactions, π – π stacking is between two open-shell cation radicals with an unpaired electron. This has led to suggestions that these two unpaired electrons may interact to form a partial intermolecular covalent bond.[10-12] Furthermore, recent work has shown that other ions present in solution, such as citrate anions in our case left-over from the AuNP synthesis and displaced from the AuNP surface, could in fact induce aggregation by acting creating "bridging attractions".[13-14] In principle, the citrate anion could act as a "cross-linker" in terms of creating attractive electrostatic interactions between the positively charged $TTF^{\bullet+}_{ads}$ ligands and the negatively charged citrate. As for vdWs attractions, although individual "bridging attractions" are of themselves quiet weak, the significant number of $TTF^{\bullet+}_{ads}$ ligands attached to the AuNP surface capable of being bridged could induce aggregation in the presence of citrate.

SI-6E: Dispersive and attractive forces that influence AuNP interactions within interfacial films

A key feature of interfacially adsorbed AuNPs is that despite being trapped vertically at the interface they may still under certain circumstances have freedom to move laterally, a property which may be used to create spatially uniform interfacial assemblies.[15-16] Considerable additional dispersive and attractive forces, of greater complexity than DLVO theory for bulk AuNP interactions, control AuNP interactions within interfacial fluid films. The interactions between NPs at fluid interfaces have been summarized succinctly by Edel and co-workers[17] and reviewed by Bresme and Oettel.[18] The complexity of these interactions means that much theoretical, simulation and experimental work remains to fully elucidate the relative importance and mechanisms of the following forces on the AuNP self-assembly process at the interface: (i) interfacial vdWs forces, that differ from bulk vdWs forces, (ii) interfacial tension stabilization, (iii) long-range dipole-dipole interactions resulting from an asymmetric counter-ion cloud, (iv) hydration forces, (v) capillary forces resulting from deformations of the interface and (vi) thermal fluctuations. The precise balance of these interparticle forces for our system allows the interfacial matrix of TTF^{0}, $TTF^{\bullet+}_{ads}$ and free $TTF^{\bullet+}$ to act as lubricating molecular glue, binding the AuNPs together, while retaining some freedom of movement to facilitate multilayer formation.

SI-7: Mechanical properties of gold metal liquid-like droplets (MeLLDs)

SI-7A: Sessile Drop Measurements

Sessile drop measurements were performed as described in the Experimental Section of the main article. The contact angles (θ_c) were measured between the droplet and a quartz surface to allow direct comparison of the relative magnitudes of the water-oil interfacial surface tension (γ) for each droplet analyzed.

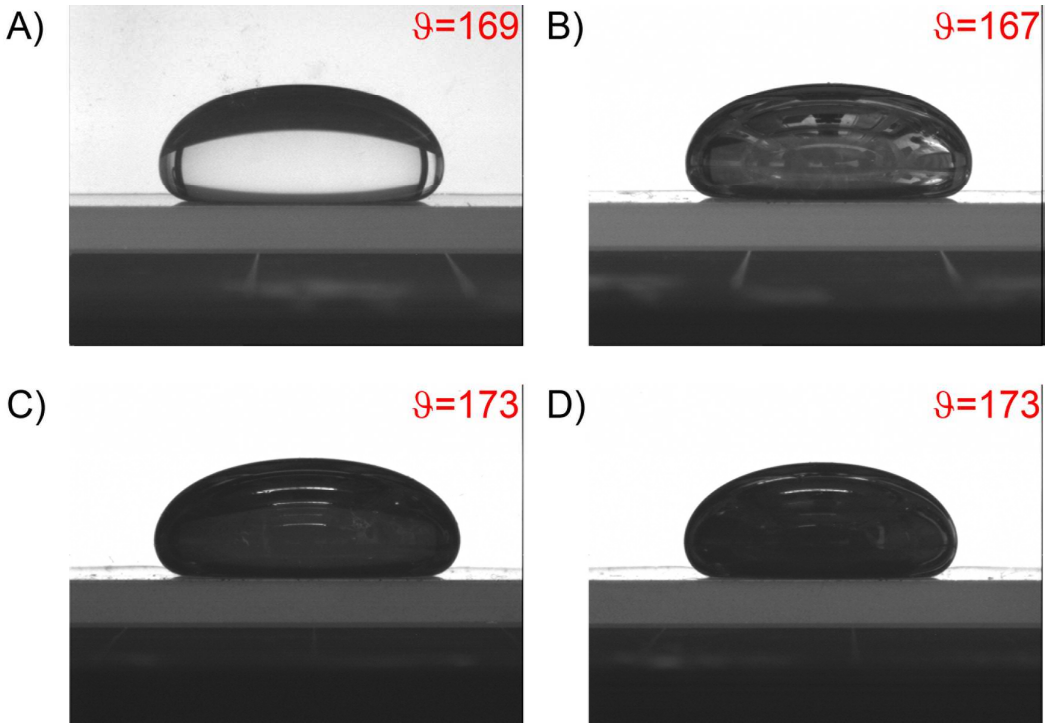

Figure S9. Images of the sessile drops, surrounded by an aqueous solution and placed on a quartz surface, of (a) a DCE droplet containing 1 mM TTF, and gold MeLLDs formed with (b) 0.5, (c) 1, and (d) 3 equivalent monolayers of AuNPs. The wetting of the glass by each droplet was determined using a Drop Shape Analyzer DSA100 (Krüss, Germany).

SI-7B: Vortex and ultrasonication of compressed MeLLDs

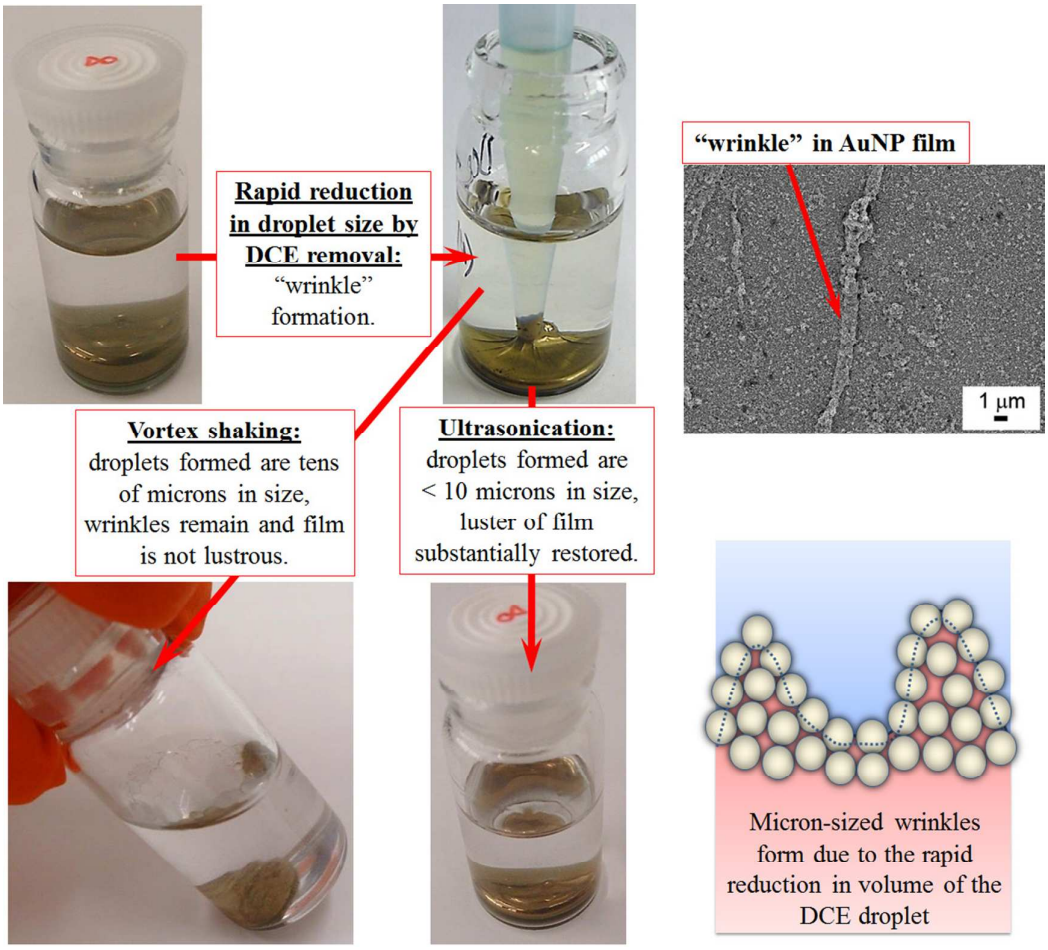

Figure S10. Images of the behavior of a gold MeLLD upon compression (*i.e.*, when the DCE is withdrawn from the droplet by a micropipette). Wrinkles or protrusions are formed on the gold MeLLD in conjunction with areas of the MeLLD that remain flat and smooth. An SEM of a typical micron sized wrinkle is shown on the top right hand side of the figure. The wrinkles remain to a large extent after vigorous shaking using a vortex shaker but the luster of the gold MeLLD is substantially restored and the wrinkles absent after ultrasonication, as discussed in the main article. The formation of the wrinkles is a kinetic effect where the AuNPs do not have time to re-arrange within the interfacial glue layer at the interface on the short timescale when DCE is withdrawn.

Supplementary References

1. Haiss, W.; Thanh, N. T. K.; Aveyard, J.; Fernig, D. G., Determination of Size and Concentration of Gold Nanoparticles from UV−Vis Spectra. *Anal. Chem.* **2007,** *79*, 4215-4221.

2. Nichols, R. J.; Burgess, I.; Young, K. L.; Zamlynny, V.; Lipkowski, J., A quantitative evaluation of the adsorption of citrate on Au(111) using SNIFTIRS. *J. Electroanal. Chem.* **2004,** *563*, 33-39.

3. Olaya, A. J.; Ge, P.; Gonthier, J. F.; Pechy, P.; Corminboeuf, C.; Girault, H. H., Four-Electron Oxygen Reduction by Tetrathiafulvalene. *J. Am. Chem. Soc.* **2011,** *133*, 12115-12123.

4. Weitz, D. A.; Oliveria, M., Fractal Structures Formed by Kinetic Aggregation of Aqueous Gold Colloids. *Phys. Rev. Lett.* **1984,** *52*, 1433-1436.

5. Ghosh, S. K.; Pal, T., Interparticle Coupling Effect on the Surface Plasmon Resonance of Gold Nanoparticles: From Theory to Applications. *Chem. Rev.* **2007,** *107*, 4797-4862.

6. Steyaert, G.; Lisa, G.; Gaillard, P.; Boss, G.; Reymond, F.; Girault, H. H.; Carrupt, P.-A.; Testa, B., Intermolecular Forces Expressed in 1,2-Dichloroethane-Water Partition Coefficients. *J. Chem. Soc., Faraday Trans.* **1997,** *93*, 401-406.

7. Trasatti, S., The Absolute Electrode Potential: An Explanatory Note. *Pure Appl. Chem.* **1986,** *58*, 955-966.

8. Su, B.; Girault, H. H., Absolute Standard Redox Potential of Monolayer-Protected Gold Nanoclusters. *J. Phys. Chem. B* **2005,** *109*, 11427-11431.

9. Jeppesen, J. O.; Nielsen, M. B.; Becher, J., Tetrathiafulvalene Cyclophanes and Cage Molecules. *Chem. Rev.* **2004,** *104*, 5115-5132.

10. Wang, F.; Wang, Y.; Wang, B.; Wang, Y.; Ma, F.; Li, Z., A Covalent Attraction between Two Molecular Cation TTF·+. *Sci. China Ser. B-Chem.* **2009,** *52*, 1980-1986.

11. Spruell, J. M.; Coskun, A.; Friedman, D. C.; Forgan, R. S.; Sarjeant, A. A.; Trabolsi, A.; Fahrenbach, A. C.; Barin, G.; Paxton, W. F.; Dey, *et al.*, Highly Stable Tetrathiafulvalene Radical Dimers in [3]Catenanes. *Nature Chem.* **2010,** *2*, 870-879.

12. Coskun, A.; Spruell, J. M.; Barin, G.; Fahrenbach, A. C.; Forgan, R. S.; Colvin, M. T.; Carmieli, R.; Benítez, D.; Tkatchouk, E.; Friedman, D. C; *et al.*,

Mechanically Stabilized Tetrathiafulvalene Radical Dimers. *J. Am. Chem. Soc.* **2011,** *133*, 4538-4547.

13. Ojea-Jiménez, I.; Puntes, V., Instability of Cationic Gold Nanoparticle Bioconjugates: The Role of Citrate Ions. *J. Am. Chem. Soc.* **2009,** *131*, 13320-13327.

14. Wang, D.; Tejerina, B.; Lagzi, I.; Kowalczyk, B.; Grzybowski, B. A., Bridging Interactions and Selective Nanoparticle Aggregation Mediated by Monovalent Cations. *ACS Nano* **2010,** *5*, 530-536.

15. Park, Y.-K.; Yoo, S.-H.; Park, S., Assembly of Highly Ordered Nanoparticle Monolayers at a Water/Hexane Interface. *Langmuir* **2007,** *23*, 10505-10510.

16. Park, Y.-K.; Park, S., Directing Close-Packing of Midnanosized Gold Nanoparticles at a Water/Hexane Interface. *Chem. Mater.* **2008,** *20*, 2388-2393.

17. Turek, V. A.; Cecchini, M. P.; Paget, J.; Kucernak, A. R.; Kornyshev, A. A.; Edel, J. B., Plasmonic Ruler at the Liquid–Liquid Interface. *ACS Nano* **2012,** *6*, 7789-7799.

18. Bresme, F.; Oettel, M., Nanoparticles at Fluid Interfaces. *J. Phys.: Condens. Matter* **2007,** *19*, 413101.